Open access • Journal Article • DOI:10.1063/5.0016230

Energetic degeneracy and electronic structures of germanium trimers doped with titanium — Source link

Le Nhan Pham, Salvy P. Russo

Institutions: RMIT University

Published on: 19 Aug 2020 - Journal of Chemical Physics (AIP Publishing)

Topics: Ground state and Coupled cluster

Energetic Degeneracy and Electronic Structures of Germanium Trimers Doped with Titanium

Le Nhan Pham*,†,‡ and Salvy P. Russo*,†

†*ARC Centre of Excellence in Exciton Science, School of Science, RMIT University, Melbourne, 3000, Australia*

‡*Department of Chemistry, The University of Dalat, 670000 Dalat, Vietnam*

E-mail: le.nhan.pham@rmit.edu.au; salvy.russo@rmit.edu.au

Phone: +61 99 25 26 01

Abstract

Geometries and electronic structures of germanium trimer clusters doped with titanium $TiGe_3^{-/0}$ were studied making use of the CASSCF/CASPT2, CCSD(T)-F12, and TPSS methods. Three used quantum chemical methods pointed out that the most stable geometries of both neutral and cationic clusters $TiGe_3^{-/0}$ have a pyramid shape (C_{3v} and C_s spatial symmetries). Two electronic states (^{2}A' and ^{2}A") of the anion were determined to be nearly degenerate and energetically competing for the anionic ground state of $TiGe_3^-$. These two states are believed to be concurrently populated in the experiment, and contribute to all visible anion photoelectron bands in the experimental spectrum. Total 14 electronic transitions starting from the ^{2}A' and ^{2}A" states were predicted to be underlying 5 out of 6 visible bands in the experimental anion photoelectron spectrum of $TiGe_3^-$. Each band was proven to be caused by multiple one-electron detachments from two populated anionic states. The last experimental band with the highest detachment energy is believed to be the result of various inner one-electron removals. Multidimensional Franck-Condon factor simulations of two first transitions where vibrational frequencies of three involved states are accessible were conducted to give more details to the lowest-ionization band.

Introduction

In the search for new materials used in semiconductor industry, germanium arises as a potential candidate for high performance materials taking part in future non-silicon transistors.[1] Several works were conducted to identify new forms and properties of pure germanium materials.[2–7] In order to discover new germanium-based counterparts and improve their expected properties, pure germanium materials are doped with a second element, usually transition or noble metals. In doing so, dozens of metal doped germanium materials were studied either experimentally or theoretically.[8–19]

Once the new materials are synthesized, several experimental techniques can be used

to characterize these new materials. Anion photoelectron (PE) spectroscopy is one of frequently used techniques for materials in the form of clusters. In principle, the synthesized clusters after being mass selected are irradiated with a laser beam of photons, leading to removals of valence electrons. The signals of removed electrons are then recorded in the anion PE spectra, and detachment energies of electrons are also determined. On the basis of detachment energies and cluster sizes, quantum chemical computations are performed subsequently to identify geometries, electronic structures, and related properties of obtained clusters.[11–14,16,18,19]

Multiconfigurational or strongly correlated characters are inherent in systems containing transition metals and their excited states, and therefore have strong effects on energetic properties of systems.[20] For pure germanium clusters and their metal doped ones, energetic degeneracy and multiconfigurational features were found to significantly contribute to the potential energy surfaces of corresponding clusters.[21–24] As a result, single reference methods (DFT, CCSD(T)) may not give reliable energetic values.[25–29] To accurately describe such systems and their excited states, the use of multireference quantum chemical methods is inevitable.[3] Such use also shed light on the dominant electronic configurations of the studied systems that single reference calculations can be based on subsequently. Hence, simultaneous utilization of both single reference and multireference methods to support and confirm results of each other are expected to be more reliable in description of non-single reference systems.[23,24,30–32]

As mentioned above, germanium clusters doped with transition metals are expected to be multiconfigurational and energetically degenerate. Based on the experimental spectroscopic data and quantum computations, multireference features were proven to be the main features of $TiGe_2^{-/0}$, and nearly degenerate electronic states are the origin of all electronic transitions causing visible bands in the experimental spectrum of $TiGe_2^-$.[23] A larger size of germanium doped with titanium ($TiGe_3^{-/0}$) was spectroscopically reported as well.[19] The anion photoelectron spectrum of $TiGe_3^-$ is more complicated than that of $TiGe_2^-$ with regard

to the number of visible bands,[19] which means that more electronic transitions were observed in the experiment. Particularly, six distinguished ionization levels were reported. The lowest one, usually corresponding to a ground-ground electronic transition, has an adiabatic detachment energy (ADE) of 1.43 eV, while its vertical detachment energy (VDE) is 1.67 eV. Five higher ionization levels have VDEs of 1.95, 2.38, 2.68, 3.20, and 3.43 eV in ascending order. For the sake of convenience, all six experimental bands are denoted by X to E in the experimental spectrum of $TiGe_3^-$ as can be seen in Figure 1.

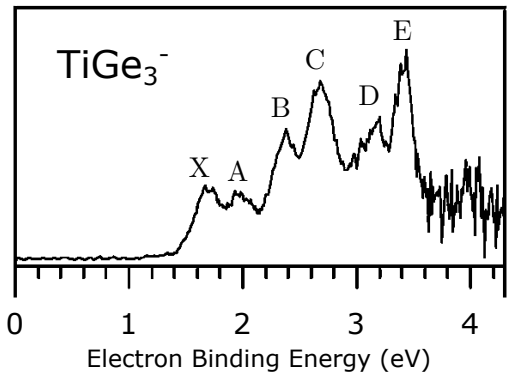

Figure 1: Experimental anion photoelectron spectrum of $TiGe_3^-$ (reproduced with permission from ref 19, Copyright 2014, RSC Publisher).

Basic explanation for the obtained experimental spectrum of $TiGe_3^-$ was made on the basis of DFT calculations.[19] A C_s tetrahedral isomer (see Figure 2c) was found to be the most stable isomer for both the neutral (^{3}A) and anion (^{2}A). Therefore, the first band X was assigned to the electronic transition $^2\text{A} \longrightarrow {}^3\text{A}$. This assignment is not clear enough because the most stable isomer of $TiGe_3^-$ belongs the C_s point-group symmetry, and hence the involved electronic states need to be more specific. Five more experimental bands corresponding to higher levels of ionization observed in the spectrum of $TiGe_3^-$ are still unexplained. Because the $TiGe_3^{-/0}$ clusters are among the smallest metal doped clusters of germanium, accurate description of such small systems will contribute to a systematic understanding of whole series doped with titanium, and will partially shed light on selection of possible DFT functionals for future study of larger clusters. Hence, we decided to study $TiGe_3^{-/0}$ by using rather high-level theory of wave function methods in combination with appropriate density functionals.

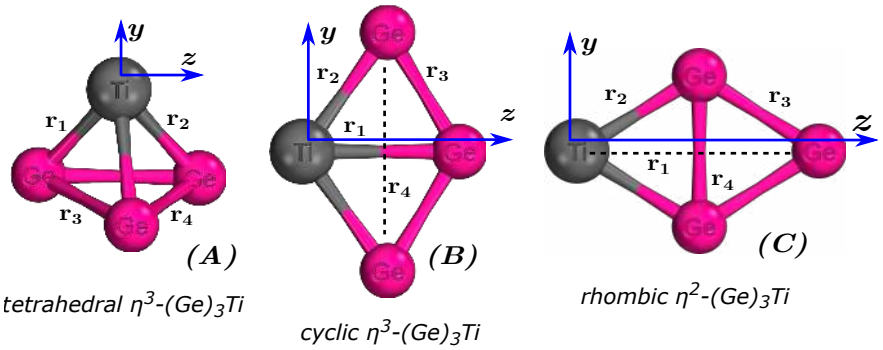

Figure 2: Three isomers of $TiGe_3^{-/0}$ and the coordinate systems used in this work.

Computational Methods

The computational process includes geometrical optimization, additional single point calculations, and Franck-Condon factor simulations. Because the difference in energy of important states are negligible, a few more calculations were conducted to assess effects of zero-point energy (ZPE) on the nearly degenerate states. To make things easier to follow, three quantum chemical programs used in this work are mentioned here first. Specifically, multiconfigurational calculations were conducted making use of the OpenMolcas code;[33] single point energies were obtained from calculations done with the Molpro program 2019;[34] the Turbomole 7.2 package[35] was employed for DFT vibrational frequencies and ZPEs.

A general geometrical pattern of atomic clusters is often unknown, and therefore the first step is to identify the most stable geometrical structure of $TiGe_3^{-/0}$. Since electronic states of $TiGe_3^{-/0}$ are expected to be multiconfigurational, geometries of $TiGe_3^{-/0}$ were optimized at the CASSCF/CASPT2 level of theory.[36] From the previous report[19] and our preliminary DFT calculations, three geometrical shapes of $TiGe_3^{-/0}$ should be considered at this level of theory. These three geometrical structures and their pre-defined coordinate systems are given in Figure 2. The CASSCF calculations need to be fed with an active space for generation of all possible configuration state functions. For $TiGe_3^{-/0}$, an active space of 15 orbitals consisting of all six valence orbitals (4s and 3d) of Ti and nine 4p ones of the Ge_3 moiety. Note that the number of electrons in the anion is higher than that in the neutral by one. Hence with

the same active space size, the numbers of electrons in the active space of the anion and the neutral have a difference of 1, being 11 and 10, respectively. For each CASSCF/CASPT2 calculation, dynamic correlation energy is computed on the top of the CASSCF wave function by implementation of the second order perturbation CASPT2. All 3p and inner core orbitals of both vanadium and germanium atoms were not taken into account (kept frozen) in the perturbative calculations. All the CASSCF/CASPT2 calculations were done in combination with the ANO-RCC basis sets contracted to [7s6p4d3f2g][37] and [6s5p3d1f][38] for vanadium and germanium, respectively.

Various single point energies of optimized electronic states were computed using the CASPT2 geometries. Single point calculations at two levels of theory (RCCSD(T)-F12[39,39] and TPSS[40]) were carried out to synergistically support the CASPT2 results. The explicitly correlated RCCSD(T)-F12 method can recover dynamic correlation energy quite well with a relatively small-size basis set in comparison to the RCCSD(T). Therefore, two triple-ζ basis sets aug-cc-pVTZ[41] and cc-PVTZ[42] were use for titanium and germanium at this level. For TPSS calculations, a larger quadruple-ζ basis set aug-cc-pVQZ-DK[41,42] was used for both Ti and Ge. Due to the importance of relativistic effects in transition metals and heavy elements, all electron scalar relativistic effects were taken into account by treatment of the second-order Douglas-Kroll-Hess Hamiltonian (DKH2).[43] Calculations of correlation energy in the RCCSD(T)-F12 implementation excludes dynamic recovery from frozen core orbitals as in the CASPT2 calculations. Unless otherwise stated, relative energies of listed states were deduced from bare electronic energies without ZPE correction because ZPEs seem not to significantly affect potential energy surfaces of small systems.

In order to do Franck-Condon factor simulations, harmonic vibrational frequencies of involved electronic states need to be provided for integration of vibrational wave functions. The frequencies of vibrations were analytically calculated at the TPSS level employing the triple-ζ def2-TZVP basis set.[44] The overlap integrals between vibrational wave functions of initial and final states were obtained with the aid of the MolFC code.[45] Analysis of vibrations

also ensures negligible contribution of ZPEs to nearly degenerate electronic states of $TiGe_3^{-/0}$.

Results and discussion

Most Stable Isomer and Electronic Ground States

The most stable geometrical and electronic structures of the anionic and neutral ground states are paramount important in elucidation of the observed $TiGe_3^-$ spectrum. This is because most of the visible bands appearing in the spectrum originate from the most stable anionic isomer and its ground state. Therefore, to ensure that findings of the most stable isomer and the ground states of $TiGe_3^{-/0}$ are reliable, energies of various electronic states were computed at three levels of theory (CASSCF/CASPT2, RCCSD(T)-F12, and TPSS) simultaneously. The Relative state energies of three probed isomers (Figure 2) are tabulated in Table 1 disclosing the most stable isomer and lowest electronic states of the anion and neutral $TiGe_3^{-/0}$. Three used methods determined that the tetrahedral η^3-$(Ge)_3Ti$ (isomer A in Figure 2) was found to be the most stable geometrical structure of the anionic and neutral $TiGe_3^{-/0}$ clusters, which is in agreement with a previous report.[19] To be more detailed, at the CASPT2 level the ^{2}A" state of the tetrahedral η^3-$(Ge)_3Ti^-$ was identified as the anionic ground state which is 0.30 and 0.47 eV more stable than the lowest low-lying states of the cyclic η^3-$(Ge)_3Ti^-$ ($^2B_2$, isomer B) and rhombic η^2-$(Ge)_3Ti^-$ ($^4B_2$, isomer C), respectively. For the neutral cluster $TiGe_3$, the ^{3}A" state of isomer A is clearly the global ground state of the neutral. Two next low-lying states ($^3B_2$ and $^3A_2$) of the isomer C are ~0.6 eV higher than the ^{3}A" state of isomer A. The RCCSD(T)-F12 and TPSS results also reinforce geometrical findings from CASPT2 optimizations. Note that for some low-lying electronic states represented by hyper open-shell electronic configurations, single-reference methods cannot treat these state wave functions, and therefore their relative energies at RCCSD(T)-F12 and TPSS are not available in Table 1.

Table 1: Relative energy of three isomers (A, B and C) and their electronic states at the three used levels of theory

isomer	sym.	state	CASPT2 geometry (Å) r1, r2, r3, r4	relative energy (eV)		
				TPSS	RCCSD(T)-F12	CASPT2
A-anion	C_s	^{2}A'	2.49, 2.43, 2.63, 2.85	0.01	0.01	0.01
		^{2}A"	2.42, 2.47, 2.78, 2.56	0.00	0.00	0.00
		^{4}A'	2.47, 2.45, 2.63, 2.84	0.45	0.79	0.60
		^{4}A"	2.53, 2.51, 2.60, 2.60	0.22	0.48	0.22
B-anion	C_{2v}	$^2A_1$	2.69, 2.51, 2.39, 4.09	0.60	0.36	0.45
		$^2B_1$	2.71, 2.47, 2.50, 4.17			1.06
		$^2B_2$	2.70, 2.44, 2.48, 4.11	0.43	0.20	0.30
		$^2A_2$	2.93, 2.49, 2.42, 3.94	0.56	0.29	0.37
		$^4A_1$	3.27, 2.53, 2.42, 3.73	0.83	1.10	0.81
		$^4B_1$	2.89, 2.49, 2.45, 4.01	0.56	0.65	0.48
		$^4B_2$	2.64, 2.45, 2.42, 4.09	0.68	0.53	0.76
		$^4A_2$	2.75, 2.52, 2.40, 4.07	0.60	0.52	0.77
C-anion	C_{2v}	$^2A_1$	4.23, 2.52, 2.45, 2.61	1.05	0.95	1.05
		$^2B_1$	4.45, 2.74, 2.42, 2.58	1.32	0.94	1.07
		$^2B_2$	4.39, 2.64, 2.43, 2.53			0.82
		$^2A_2$	4.39, 2.66, 2.42, 2.55	2.24	2.04	0.70
		$^4A_1$	3.26, 2.53, 2.42, 3.73	0.83	1.10	0.81
		$^4B_1$	4.47, 2.73, 2.42, 2.60	0.57	0.96	0.70
		$^4B_2$	4.41, 2.65, 2.43, 2.53	0.38	0.81	0.47
		$^4A_2$	4.42, 2.70, 2.42, 2.58	0.86	1.15	0.69
A-neutral	C_s	^{1}A'	2.44, 2.46, 2.65, 2.69	2.22	1.63	1.64
		^{1}A"	2.45, 2.45, 2.69, 2.61			1.34
		^{3}A'	2.51, 2.50, 2.83, 2.44	2.14	2.38	2.00
		^{3}A"	2.46, 2.46, 2.64, 2.64	1.39	1.63	1.27
B-neutral	C_{2v}	$^1A_1$	2.52, 2.39, 2.59, 4.28	2.49	1.86	3.11
		$^1B_1$	2.73, 2.49, 2.49, 4.15			2.55
		$^1B_2$	2.60, 2.51, 2.43, 4.21			2.50
		$^1A_2$	2.72, 2.55, 2.39, 4.12			2.57
		$^3A_1$	2.86, 2.63, 2.40, 4.12	2.74	2.84	2.58
		$^3B_1$	2.87, 2.48, 2.45, 4.01	2.40	2.46	2.26
		$^3B_2$	2.54, 2.50, 2.44, 4.23	2.32	2.36	2.14

Continued on next page

Table 1 – continued from previous page

isomer	sym.	state	CASPT2 geometry (Å) r1, r2, r3, r4	relative energy (eV)		
				TPSS	RCCSD(T)-F12	CASPT2
		$^3A_2$	2.70, 2.57, 2.38, 4.13	2.36	2.68	2.23
C-neutral	C_{2v}	$^1A_1$	4.03, 2.46, 2.44, 2.78	2.49	2.30	2.28
		$^1B_1$	4.45, 2.61, 2.47, 2.43			2.97
		$^1B_2$	4.20, 2.49, 2.45, 2.62			2.47
		$^1A_2$	4.39, 2.56, 2.47, 2.46			2.52
		$^3A_1$	4.24, 2.63, 2.40, 2.71	2.21	2.60	2.12
		$^3B_1$	4.22, 2.66, 2.38, 2.75	1.89	2.64	2.18
		$^3B_2$	4.21, 2.58, 2.41, 2.66	1.99	2.43	1.89
		$^3A_2$	4.23, 2.56, 2.41, 2.62	1.86	2.38	1.89

From Table 1, one can see that two anionic states ^{2}A' and ^{2}A" of the isomer A are nearly degenerate, and compete with each other for the ground state of the anion $TiGe_3^-$. The difference in energy of these two states is ∼0.01 eV, in which the ^{2}A" state is slightly more stable than the ^{2}A' one. Because the difference is insignificant, we need to examine the effect of ZPEs on energies of these two competitive states. Relative energies corrected with the TPSS ZPEs of the two states ^{2}A' and ^{2}A" are given in Table 2. Obviously, ZPE does not substantially affect energy of the two nearly degenerate states. Especially, at the CASPT2 level of theory, the difference is almost close to zero (0.002 eV). Therefore, it is strongly believed that these two nearly degenerate states were concurrently populated in the experiment, and underwent one-electron removals simultaneously.

Table 2: Effects of zero-point energy (ZPE) on the energetic minima of two lowest anionic states ^{2}A' and ^{2}A"

state	CASPT2 (eV)		CCSD(T)-F12 (eV)		TPSS (eV)	
	without ZPE	with ZPE	without ZPE	with ZPE	without ZPE	with ZPE
^{2}A"	0.00	0.00	0.00	0.00	0.00	0.00
^{2}A'	0.01	0.00[a]	0.01	0.01	0.01	0.01

[a] The actual value is 0.002

Let us recapitulate a few main points related to geometrical structures and electronic ground states of $TiGe_3^{-/0}$ identified thus far. The most stable geometrical structures of $TiGe_3^{-/0}$ have a pyramid form (see Figure 2) with a low symmetry group C_s. However, the C_s symmetry is only true for the geometries of two lowest states (^{2}A' and ^{2}A") of the anionic cluster $TiGe_3^-$. The actual symmetry point group of the neutral cluster belongs to a higher symmetry point group C_{3v}. Therefore, the correct electronic ground state of the neutral should be ^{3}E instead of ^{3}A". It is worth noting that while the anion has nearly degenerate electronic states (^{2}A' and ^{2}A") vying for the ground state, the neural has only one state ^{3}E (^{3}A" in C_s) being the ground state. Explanations for difference between symmetry of the anionic and neutral ground states, and for the degeneracy in the most stable anionic cluster will be provided later in detail once the electronic structures of these states are analyzed.

Electronic Structures and Possible Electron Detachments

Electronic structures play an import role in prediction of possible electronic transitions causing visible bands in the experimental spectrum of $TiGe_3^-$. Understanding of electronic structures will unveil insights into geometrical properties and energetic degeneracy in the studied clusters $TiGe_3^{-/0}$. For the sake of electronic analysis, the dominant electronic configurations of the anionic and neutral ground states, and of several low-lying ones extracted from the CASSCF wave functions are provided in Table 3.

Table 3: Leading Electronic Configurations Obtained from the CASSCF wave functions and Predicted Electronic Transitions. Dominant AO components of ionized orbitals are noted in brackets

state	leading electronic configuration	weight (%)[b]	ionization	ionized orbital
1^2A'	$32a'^2\ 33a'^2\ 34a'^2\ 35a'^2\ 36a'^2\ 37a'^{\uparrow}\ 38a'^0\ 21a''^2\ 22a''^2\ 23a''^2\ 24a''^0$	71		
1^2A''	$32a'^2\ 33a'^2\ 34a'^2\ 35a'^2\ 36a'^2\ 37a'^2\ 38a'^0\ 21a''^2\ 22a''^2\ 23a''^{\uparrow}\ 24a''^0$	72		
1^1A'	$32a'^2\ 33a'^2\ 34a'^2\ 35a'^2\ 36a'^2\ 37a'^0\ 38a'^0\ 21a''^2\ 22a''^2\ 23a''^2\ 24a''^0$	55	1^2A' $\longrightarrow$ 1^1A'	37a' [Ti $3d_{x^2-y^2}$, Ti $3d_{yz}$]
2^1A'	$32a'^2\ 33a'^2\ 34a'^2\ 35a'^2\ 36a'^2\ 37a'^2\ 38a'^0\ 21a''^2\ 22a''^2\ 23a''^0\ 24a''^0$	55	1^2A'' $\longrightarrow$ 2^1A'	23a'' [Ti $3d_{xz}$]
3^1A'	$32a'^2\ 33a'^2\ 34a'^2\ 35a'^2\ 36a'^2\ 37a'^2\ 38a'^0\ 21a''^2\ 22a''^{\uparrow}\ 23a''^{\downarrow}\ 24a''^0$	33		
4^1A'	$32a'^2\ 33a'^2\ 34a'^2\ 35a'^2\ 36a'^{\uparrow}\ 37a'^{\downarrow}\ 38a'^0\ 21a''^2\ 22a''^2\ 23a''^2\ 24a''^0$	57		
1^1A''	$32a'^2\ 33a'^2\ 34a'^2\ 35a'^2\ 36a'^2\ 37a'^{\uparrow}\ 38a'^0\ 21a''^2\ 22a''^2\ 23a''^{\downarrow}\ 24a''^0$	71	1^2A' $\longrightarrow$ 1^1A''	23a'' [Ti $3d_{xz}$]
2^1A''	$32a'^2\ 33a'^2\ 34a'^2\ 35a'^2\ 36a'^2\ 37a'^{\uparrow}\ 38a'^0\ 21a''^2\ 22a''^{\downarrow}\ 23a''^2\ 24a''^0$	37	1^2A' $\longrightarrow$ 2^1A''	22a'' [Ge 4p]
3^1A''	$32a'^2\ 33a'^2\ 34a'^2\ 35a'^2\ 36a'^{\uparrow}\ 37a'^2\ 38a'^0\ 21a''^2\ 22a''^{\downarrow}\ 23a''^2\ 24a''^0$	37		
4^1A''	$32a'^2\ 33a'^2\ 34a'^2\ 35a'^2\ 36a'^2\ 37a'^0\ 38a'^{\uparrow}\ 21a''^2\ 22a''^2\ 23a''^{\downarrow}\ 24a''^0$	60		
1^3A'	$32a'^2\ 33a'^2\ 34a'^2\ 35a'^2\ 36a'^2\ 37a'^2\ 38a'^0\ 21a''^2\ 22a''^{\uparrow}\ 23a''^{\uparrow}\ 24a''^0$	69	1^2A'' $\longrightarrow$ 1^3A'	22a'' [Ge 4p]
2^3A'	$32a'^2\ 33a'^2\ 34a'^2\ 35a'^2\ 36a'^{\uparrow}\ 37a'^{\uparrow}\ 38a'^0\ 21a''^2\ 22a''^2\ 23a''^2\ 24a''^0$	67	1^2A' $\longrightarrow$ 2^3A'	36a' [Ge 4p]
3^3A'	$32a'^2\ 33a'^2\ 34a'^2\ 35a'^{\uparrow}\ 36a'^2\ 37a'^{\uparrow}\ 38a'^0\ 21a''^2\ 22a''^2\ 23a''^2\ 24a''^0$	51	1^2A' $\longrightarrow$ 3^3A'	35a' [Ti 4s, Ge 4p]
4^3A'	$32a'^2\ 33a'^2\ 34a'^2\ 35a'^2\ 36a'^2\ 37a'^0\ 38a'^0\ 21a''^2\ 22a''^2\ 23a''^{\uparrow}\ 24a''^{\uparrow}$	53		
5^3A'	$32a'^2\ 33a'^2\ 34a'^2\ 35a'^2\ 36a'^2\ 37a'^{\uparrow}\ 38a'^{\uparrow}\ 21a''^2\ 22a''^2\ 23a''^0\ 24a''^0$	52		
6^3A'	$32a'^2\ 33a'^2\ 34a'^2\ 35a'^2\ 36a'^2\ 37a'^0\ 38a'^0\ 21a''^2\ 22a''^2\ 23a''^{\uparrow}\ 24a''^{\uparrow}$	24		
7^3A'	$32a'^2\ 33a'^2\ 34a'^{\uparrow}\ 35a'^2\ 36a'^2\ 37a'^{\uparrow}\ 38a'^0\ 21a''^2\ 22a''^2\ 23a''^2\ 24a''^0$	39	1^2A' $\longrightarrow$ 7^3A'	34a' [Ge 4p]
1^3A''	$32a'^2\ 33a'^2\ 34a'^2\ 35a'^2\ 36a'^2\ 37a'^{\uparrow}\ 38a'^0\ 21a''^2\ 22a''^2\ 23a''^{\uparrow}\ 24a''^0$	69	1^2A'' $\longrightarrow$ 1^3A''	37a' [Ti $3d_{x^2-y^2}$, Ti $3d_{yz}$]
			1^2A' $\longrightarrow$ 1^3A''	23a'' [Ti $3d_{xz}$]
2^3A''	$32a'^2\ 33a'^2\ 34a'^2\ 35a'^2\ 36a'^{\uparrow}\ 37a'^2\ 38a'^0\ 21a''^2\ 22a''^2\ 23a''^{\uparrow}\ 24a''^0$	56	1^2A'' $\longrightarrow$ 2^3A''	36a' [Ge 4p]
3^3A''	$32a'^2\ 33a'^2\ 34a'^2\ 35a'^2\ 36a'^2\ 37a'^{\uparrow}\ 38a'^0\ 21a''^2\ 22a''^{\uparrow}\ 23a''^2\ 24a''^0$	39	1^2A' $\longrightarrow$ 3^3A''	22a'' [Ge 4p]

Continued on next page

Table 3 – continued from previous page

state	leading electronic configuration	weight (%)[b]	ionization	ionized orbital
4^3A"	32a'^{2} 33a'^{2} 34a'^{2} 35a'$^\uparrow$ 36a'^{2} 37a'^{2} 38a'^{0} 21a"^{2} 22a"^{2} 23a"$^\uparrow$ 24a"^{0}	65	1^2A" ⟶ 4^3A"	35a' [Ti 4s, Ge 4p]
5^3A"	32a'^{2} 33a'^{2} 34a'^{2} 35a'^{2} 36a'^{2} 37a'^{0} 38a'$^\uparrow$ 21a"^{2} 22a"^{2} 23a"$^\uparrow$ 24a"^{0}	43		
6^3A"	32a'^{2} 33a'^{2} 34a'$^\uparrow$ 35a'^{2} 36a'^{2} 37a'^{2} 38a'^{0} 21a"^{2} 22a"^{2} 23a"$^\uparrow$ 24a"^{0}	29	1^2A" ⟶ 6^3A"	34a' [Ge 4p]
7^3A"	32a'^{2} 33a'^{2} 34a'^{2} 35a'^{2} 36a'$^\uparrow$ 37a'^{2} 38a'^{0} 21a"^{2} 22a"$^\uparrow$ 23a"^{2} 24a"^{0}	66		
8^3A'	32a'^{2} 33a'$^\uparrow$ 34a'^{2} 35a'^{2} 36a'^{2} 37a'$^\uparrow$ 38a'^{0} 21a"^{2} 22a"^{2} 23a"^{2} 24a"^{0}		1^2A' ⟶ 8^3A'	33a' [Ge 4s]
9^3A'	32a'$^\uparrow$ 33a'^{2} 34a'^{2} 35a'^{2} 36a'^{2} 37a'$^\uparrow$ 38a'^{0} 21a"^{2} 22a"^{2} 23a"^{2} 24a"^{0}		1^2A' ⟶ 9^3A'	32a' [Ge 4s]
10^3A'	32a'^{2} 33a'^{2} 34a'^{2} 35a'^{2} 36a'^{2} 37a'^{2} 38a'^{0} 21a"$^\uparrow$ 22a"^{2} 23a"$^\uparrow$ 24a"^{0}		1^2A" ⟶ 10^3A'	21a" [Ge 4s]
8^3A"	32a'^{2} 33a'$^\uparrow$ 34a'^{2} 35a'^{2} 36a'^{2} 37a'^{2} 38a'^{0} 21a"^{2} 22a"^{2} 23a"$^\uparrow$ 24a"^{0}		1^2A" ⟶ 8^3A"	33a' [Ge 4s]
9^3A"	32a'$^\uparrow$ 33a'^{2} 34a'^{2} 35a'^{2} 36a'^{2} 37a'^{2} 38a'^{0} 21a"^{2} 22a"^{2} 23a"$^\uparrow$ 24a"^{0}		1^2A" ⟶ 9^3A"	32a' [Ge 4s]
10^3A"	32a'^{2} 33a'^{2} 34a'^{2} 35a'^{2} 36a'^{2} 37a'$^\uparrow$ 38a'^{0} 21a"$^\uparrow$ 22a"^{2} 23a"^{2} 24a"^{0}		1^2A' ⟶ 10^3A"	21a" [Ge 4s]

[b] Some higher excited states are predicted by removing one electron from inner MOs of two lowest anionic states ^{2}A' and ^{2}A", and hence the coefficient weights are not available

Leading electronic configurations of the two lowest doublet states of the anion $TiGe_3^-$ are given in Table 3. Depending on irreducible representations of the sole singly occupied active molecular orbital (MO) in the active space of these states, the total symmetry feature of each state is determined correspondingly. A close look at the active orbitals reveals that these MOs are clearly constructed by hybridization of germanium (4p) and chromium (3d and 4s) valence orbitals. In other words, chemical bonds between the metal titanium atom and germanium ones are formed, and such chemical bonds make the clusters $TiGe_3^{-/0}$ chemically stable. In detail, two hybridization types between metallic valence atomic orbitals (AOs) and germanium 4p ones can be recognized: i) hybridized MOs formed by Ti 4s and Ge 4p AOs and ii) by Ti 3d and Ge 4p AOs. The former can be seen in MOs 35a' in the leading configurations of the two lowest anionic states. The remaining occupied active MOs (34a', 36a', 37a', 22a", and 23a") of the two lowest anionic electronic states are categorized as the latter.

A clear understanding of MO components will aid us in prediction of one-electron removal ordering. Among the abovementioned MOs, two active MOs 37a' and 23a" are dominantly contributed by the metallic AOs of titanium, whereas the active MOs 34a', 36a' and 22a" have more characteristics of Ge 4p AOs. To be more specific, the metallic AOs $3d_{x^2-y^2}$ and $3d_{yz}$ are found to be primary in the MOs 37a', while a major part of $3d_{xz}$ is present in the MOs 23a". With a bit difference, the 35a' MOs have equally large components of the Ti 4s and Ge 4p AOs. The other active MOs (34a', 36a', and 22a") are composed of smaller parts from the metallic AOs of Ti, which means these MOs are expected to have more impacts from the Ge 4p AOs. To have an intuitive view on the characteristics of all active MOs in the two degenerate anionic states, the visualization of these MOs is pictorially presented in Figure 3. For the purpose of prediction on deeper electron removals, three more MOs (32a', 33a', and 21a") of each anionic state are also plotted in Figure 3. These three MOs mainly originate from three 4s AOs of germanium atoms. By checking leading configurations of the remaining states in Table 3 and orbital plots in Figure 3, one can derive electronic properties

of corresponding states qualitatively.

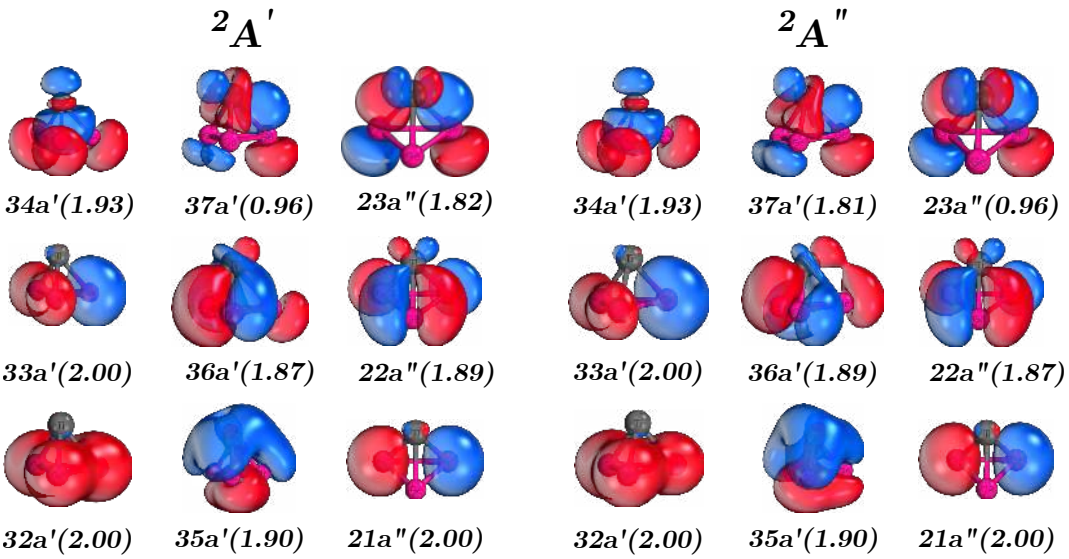

Figure 3: Occupied orbitals in the active space and three additional 4s(Ge) hybrid ones of the two lowest anionic states ^{2}A' and ^{2}A". The orbitals are obtained from CASSCF wave functions. Occupation numbers are noted in parentheses. The titanium atom is on the top of the tetrahedral cluster.

From electronic analysis of MOs above, the energetic ordering of one-electron removals occurring in the experiment can be roughly estimated. Fundamentally, MOs dominantly composed of metallic AOs tend to undergo one-electron detachments first, and vice versa. With that in mind, we can deduce that for one of the two anionic states (^{2}A' and ^{2}A") one-electron removals are expected to happen to two MOs 37a' and 23a" with dominant metallic features first. Alternatively stated, electron binding energies of single electrons located in these two MOs are estimated to be lowest. Signals of these removed electrons are often recorded as X bands in the experiment. In total, five electronic transitions starting from the two degenerate anionic states ^{2}A' and ^{2}A" were computationally predicted. These electronic transitions are presented as 1^2A' $\longrightarrow$ 1^1A', 1^2A" $\longrightarrow$ 2^1A', 1^2A' $\longrightarrow$ 1^1A", 1^2A" $\longrightarrow$ 1^3A", and 1^2A' $\longrightarrow$ 1^3A" in Table 3. Note that two separate one-electron detachments can occur in the MO 23a" of the ^{2}A' state obtained from analysis of the CASSCF state wave functions.

Conversely, electrons from the MOs characterized with larger contributions of the Ge 4p

AOs have a propensity to be removed with higher detachment energies. Therefore, three occupied MOs in the active space 34a', 36a', and 22a" of each anionic state need higher energy of photon beams to be detached. As a result, the electron detachments from these MOs are believed to be responsible for higher-energy bands in the experimental spectrum of $TiGe_3^-$. At least seven electronic transitions were identified to have involvement with one-electron removals from these three orbitals (see Table 3). In addition, one other MO (35a') has large part of the Ge 4p AOs, and hence is expected to have high detachment energy values. Because this MO is occupied in the leading electronic configuration of the states ^{2}A' and ^{2}A", two more electronic transitions 1^2A' $\longrightarrow$ 3^3A' and 1^2A" $\longrightarrow$ 4^3A" were predicted from our CASSCF calculations. Apart from aforementioned MOs in the active space, three more MOs beyond the active space of each anionic state were further used for prediction of more six inner one-electron removals responsible for the experimental band with very high electron binding energy that outer one-electron detachments cannot be attributed to.

As discussed above, symmetry point groups of the clusters are transformed from C_s to C_{3v} under the removals of one electron in the two electronic transitions 1^2A' $\longrightarrow$ 1^3A" and 1^2A" $\longrightarrow$ 1^3A". The highest symmetry point group that both the anion and neutral can possess is C_{3v}. Considering the electronic structure of the anion in its highest symmetry point group, one can deduce that there will be two 2-fold degenerate MOs in electronic configurations of any doublet state (see Figure 4). Depending on electron occupation schemes of the HOMO pair, two degenerate electronic states are expected to be simultaneously generated. In this instance, Jahn-Teller effects are expected to occur and distort the C_{3v} geometry of the anion. Two geometrical distortion directions corresponding to two electron occupation schemes lead to two lower-symmetry states within the C_s point group. This is what we obtained from CASPT2 optimization of the anionic cluster $TiGe_3^-$.

For the neutral, energetic degeneracy of states cannot happen in the triple ground state ^{3}E (^{3}A" in C_s). Two unpaired electrons occupy two two-fold degenerate HOMOs, and therefore there will be no Jahn-Teller distortion. As a result, symmetry of the triplet neutral ground

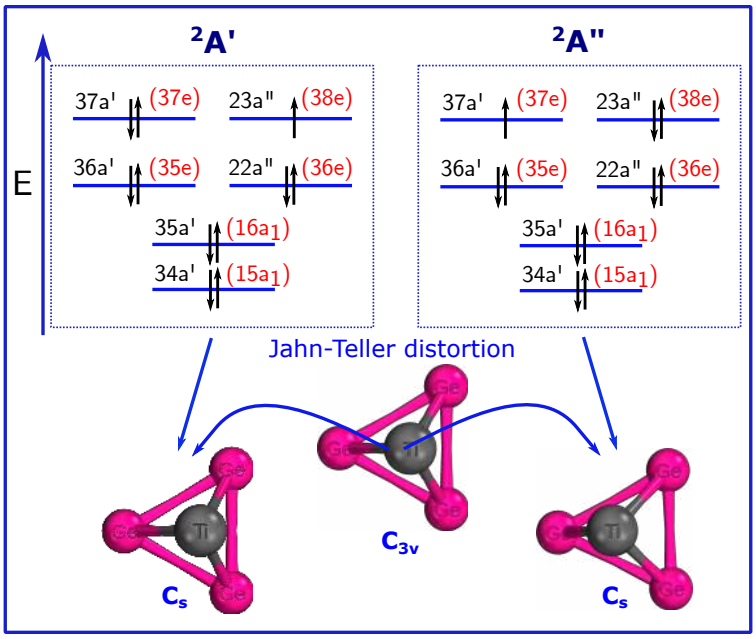

Figure 4: MO diagrams of the two-fold degenerate anionic states ^{2}A' and ^{2}A" in in the C_{3v} geometry and the Jahn-Teller effect causing geometrical distortion. The black (red) orbital labels are noted with respect to the C_s (C_{3v}) spatial symmetry. Only occupied MOs in the active space are presented.

state is unchanged, being C_{3v}. The MO diagram of this neutral ground state is provided in Figure 5. In addition, the MO diagrams of several ^{3}A" excited states are given as well. Each of these excited state, one by one, theoretically has its corresponding degenerate state once permutations of electron occupation are applied to two-fold degenerate MOs. As a result Jahn-Teller effects are expected to happen to these states, and their relaxation geometries will be constrained within the C_s spatial symmetry. A further study of Jahn-Teller effects on excited states is of future interest.

Anion Photoelectron Band Assignments

On the basis of electronic structures, energetic orderings of several predicted one-electron detachments can be roughly estimated and subsequently used for assignments of visible bands in the experimental anion PE spectrum of TiG_3^-. The general idea is that detachments of one electron from MOs resulting from hybridization of major metal AOs will be taking place

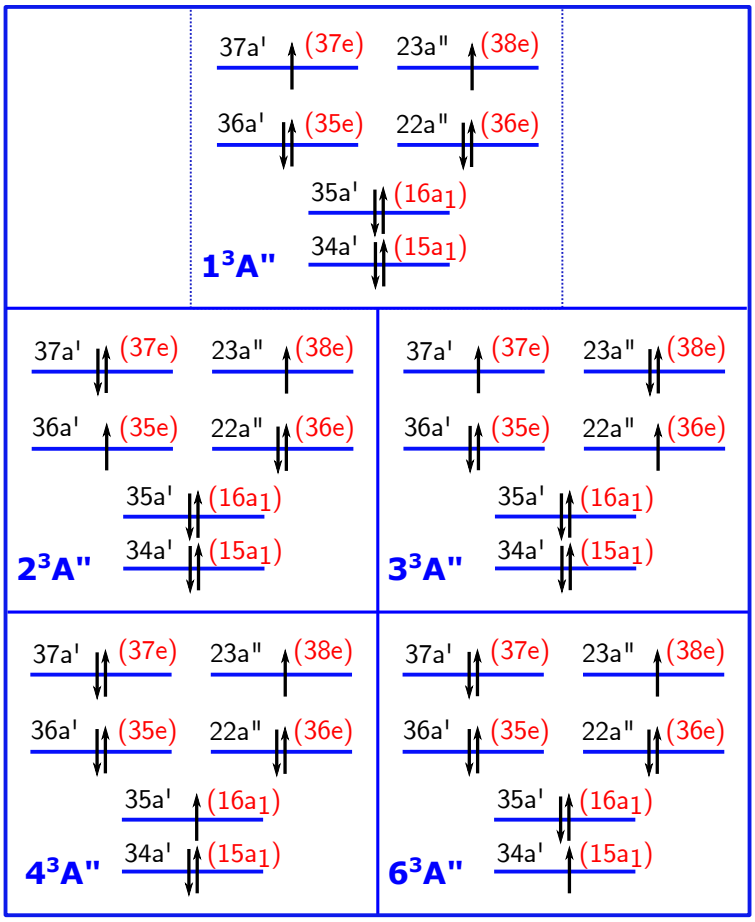

Figure 5: MO diagrams of the neutral ground state and its low-lying states in the C_{3v} geometry. The black (red) orbital labels are noted with respect to the C_s (C_{3v}) spatial symmetry. Only occupied MOs in the active space are presented.

at lower photon energy, and therefore will be reponsible for PE bands with lower binding energies. Those MOs comprised of large parts of Ge 4p AOs will have higher ionization energies, and will be causing higher-energy PE bands. In conjunction with calculated ADEs and VDEs, PE bands in the spectrum of $TiGe_3^-$ will be explained and assigned. Because two lowest anionic states (^{2}A' and ^{2}A") were determined to be energetically degenerate and simultaneously populated in the experiment, all experimental bands in the anion PE spectrum of $TiGe_3^-$ are considered based on these two states.

In the anion PE spectrum of $TiGe_3^-$, the lowest band, labelled with X in Figure 1, ranges from ~1.40 to ~1.8 eV. Conventionally, the X band is attributed to one-electron transitions from the anionic ground state to the neutral one. Interestingly, two low-lying

degenerate states (^{2}A' and ^{2}A") of the anion are known to be competing for the anionic ground state, and hence the removals of one-electron from these two anionic states to form the neutral ground state ^{3}A" are apparently reponsible for the X band. Our calculations show that the CASPT2 ADEs of two electronic transitions ^{2}A" $\longrightarrow$ ^{3}A" and ^{2}A' $\longrightarrow$ ^{3}A" are ∼1.27 eV which is ∼0.16 eV lower than the experimental ADE of the X band, being 1.43 eV. The experimental VDE of this band was determined to be 1.67 eV, and as usual the CASPT values of the ground-ground transitions are seriously underestimated for the lowest band. In this situation, single reference methods often give better theoretical values. Indeed, the RCCSD(T)-F12 VDEs are ∼1.70 eV, which is 0.03 eV deviating from the experimental VDE of 1.67 eV. The TPSS results for this band are also acceptedly reasonable with a deviation of ∼0.20 eV from the experimental values. Two ground-ground electronic transitions, their detachment energies, and experimental ones of the X band are presented in Table 4. Note that two one-electron removals causing the X band involve MOs with large hybridization compositions of Ti 3d AOs (see Table 3). There are three more one-electron removals originating from MOs characterized with dominant metal AOs as well, and therefore these electron removals are believed to take part in producing signals of the X band. The VDEs of these three transitions (1^2A' $\longrightarrow$ 1^1A', 1^2A" $\longrightarrow$ 2^1A', and 1^2A' $\longrightarrow$ 1^1A") identified at the CASPT2 level are 1.78, 1.70, and 1.74 eV which all point to the experimental value (1.67 eV). The good agreement between the experimental and calculated VDEs strongly supports the involvement of these three electronic transitions in the X band. In total, five electronic transitions were proven to concurrently arise under the irradiation of the experimental photon beam and give rise to the X band.

The next band in the anion PE spectrum of TiG_3^- was recorded at 1.95 eV, noted as A in Figure 1. Two electronic transitions 1^2A" $\longrightarrow$ 1^3A' and 1^2A' $\longrightarrow$ 2^3A' were found to be energetically befitting of this band at the CASPT2 level. To be more detailed, the CASPT2 VDEs of these two transitions are determined to be 2.08 eV, being in good correlation with the experimental VDE of 1.95 eV. Therefore, these two electronic transitions are believed

to underlie the A band. In contrast to the CASPT2 values, the VDEs obtained from single reference methods (TPSS and RCCSD(T)-F12) are quite overestimated (see Table 4). Such inaccuracy produced at single configuration levels of theory in treatment of excited sates and systems containing transition metals are not unexpected due to complicated wave functions of treated systems and correlated electron effects.

An inner ionization level of $TiGe_3^-$ was experimentally determined to be 2.38 eV, being ~0.40 eV vertically higher the A band. In Table 4, three electronic transitions starting from two competitive anionic ground state ^{2}A' and ^{2}A" to both singlet and triplet triplet states (2^1A", 2^3A", and 3^3A") have the CASPT2 VDE values of ~2.35 eV lying within the error bar (0.08 eV) of experimental VDE. Without a doubt, these three low-lying states of the neutral were assigned to the band B. From this level of excitation, energies of low-lying states cannot be accessed from the single configuration formulations due to wave function convergence issues and controlling.

Two more visible bands in the experimental spectrum of $TiGe_3^-$ can be energetically assigned within the scope of our used active space orbital. The lower one has a VDE of 2.68 eV, and the higher one 3.20 eV. The initial states are clearly two lowest anionic states as mentioned above. The final neutral states should be formed by one-electron removals from deeper anionic MOs. Intuitively, from the MO diagrams of two anionic states ^{2}A' and ^{2}A" in Figure 4 one can predict electron removals can happen to two inner MOs 35a' and 34a' of the ^{2}A' and ^{2}A" states. Our CASPT2 calculations found four electronic transitions starting from these MOs whose calculated VDEs are in good correlation with the experiment. Specifically, for the C band the CASPT2 VDEs of two transitions 1^2A' $\longrightarrow$ 3^3A' and 1^2A" $\longrightarrow$ 4^3A" are 2.59 and 2.72 eV, respectively. In comparison to the experimental VDE of the C band (2.68 eV), the errors of two calculated energies are in a range from 0.04 to 0.09 eV, which is quite convincing for assignments of the C band to two mentioned electronic transitions. Similarly, two transitions 1^2A' $\longrightarrow$ 7^3A' and 1^2A" $\longrightarrow$ 6^3A" with the calculated VDEs of 3.16 and 3.09 eV were ascribed to the appearance of the D band centered at 3.20 eV in the

Table 4: Theoretical and experimental detachment energies of five bands from X to D in the experimetal PE spectrum of $TiGe_3^-$.

state	relative energy (eV)[c]			transition	expt.[c]	band
	TPSS	RCCSD(T)-F12	CASPT2			
1^2A"	0.00	0.00	0.00			
1^2A'	0.01	0.01	0.01			
1^1A'	2.07	1.47	1.78	1^2A' ⟶ 1^1A'	1.67	X
	(2.13)	(1.62)	(1.64)		(1.43)	
2^1A'			1.70	1^2A" ⟶ 2^1A'	1.67	X
3^1A'			2.34			
4^1A'			2.59			
1^1A"			1.74	1^2A' ⟶ 1^1A"	1.67	X
			(1.65)		(1.43)	
2^1A''			2.42	1^2A' ⟶ 2^1A"	2.38	B
3^1A''			2.73			
4^1A"			2.92			
1^3A'	2.23	2.49	2.08	1^2A" ⟶ 1^3A'	1.95	A
	(2.14)	(2.37)	(2.00)			
2^3A'			2.08	1^2A' ⟶ 2^3A'	1.95	A
3^3A'			2.59	1^2A' ⟶ 3^3A'	2.68	C
4^3A'			2.67			
5^3A'			2.75			
6^3A'			3.01			
7^3A'			3.16	1^2A' ⟶ 7^3A'	3.20	D
1^3A"	1.48	1.71	1.34	1^2A" ⟶ 1^3A"	1.67	X
	(1.39)	(1.63)	(1.27)		(1.43)	
	1.46	1.69	1.33	1^2A' ⟶ 1^3A"	1.67	X
	(1.38)	(1.62)	(1.26)		(1.43)	
2^3A"			2.37	1^2A" ⟶ 2^3A"	2.38	B
3^3A"			2.33	1^2A' ⟶ 3^3A"	2.38	B
4^3A"			2.72	1^2A" ⟶ 4^3A"	2.68	C
5^3A"			2.74			
6^3A"			3.09	1^2A" ⟶ 6^3A"	3.20	D
7^3A"			3.17			

[c] ADE values in parentheses

spectrum.

Apparently, an additional visible band, represented by E in Figure 1, was recorded at a higher electron binding energy of 3.43 eV in the experimental spectrum of $TiGe_3^-$. To fully

theoretically probe this band, a larger active space of ⩾18 MOs must be employed in the CASSCF/CASPT2 calculations. The inclusion of ⩾18 MOs would be super computationally expensive. Thus, the CASPT2 VDEs of inner electronic transitions involving deeper one-electron removals are not computed. Only possible one-electron transitions, which do not violate the selection rules in anion photoelectron spectroscopy and originate from inner MOs of the two lowest anionic ^{2}A' and ^{2}A" states, are predicted. These one-electron transitions, electronic features of initial and final states, and ionized orbitals can be found in Table 3. All ionized MOs causing these transitions are mainly consisted of the Ge 4s AOs (see Figure 3), leading us to an estimation that their detachment energies will be quite high. As a result, multiple electronic transitions with involvement of these MOs are believed to generate spectroscopic signals of the E band and higher ones if possibly observed.

Franck-Condon Factor Simulations

Multidimensional Franck-Condon factor simulations of transitions whose harmonic vibrations of involved states are accessible at the TPSS level were conducted to reveal more insights into vibronic properties of the the experimental bands. Becasue each experimental band was proven to be caused by multiple electronic transitions, the simulation of a specific band needs vibrational frequencies of multiple initial and final states. However, several final states are excited states and their harmonic vibrations cannot be accessed at the DFT level. As a result, only two simulations were carried out for the X band, where the harmonic vibrational frequencies of two lowest anionic states and the neutral ground state can be obtained. These two simulations are visualized in Figture 6.

Our simulation results show that each progression is basically the result of several vibrational transitions between the initial and final states of various modes, but the 133 cm^{-1} mode is the main contribution. We also see that not only the 0-0 transition of this mode gives non zero integrals between two vibrational wave functions but higher excited vibrational states do the same, even giving rather high values of integrals. This vibrational mode

combines harmonic displacements of all atoms (see vectors in the insets of Figure 6). Such displacements can be explained partly by the detachments of one-electrons from the MOs delocalized over the cluster. The vibrational direction of Ti is exactly the same with the relaxation direction of the anion once one electron is removed from the HOMOs of $TiGe_3^-$.

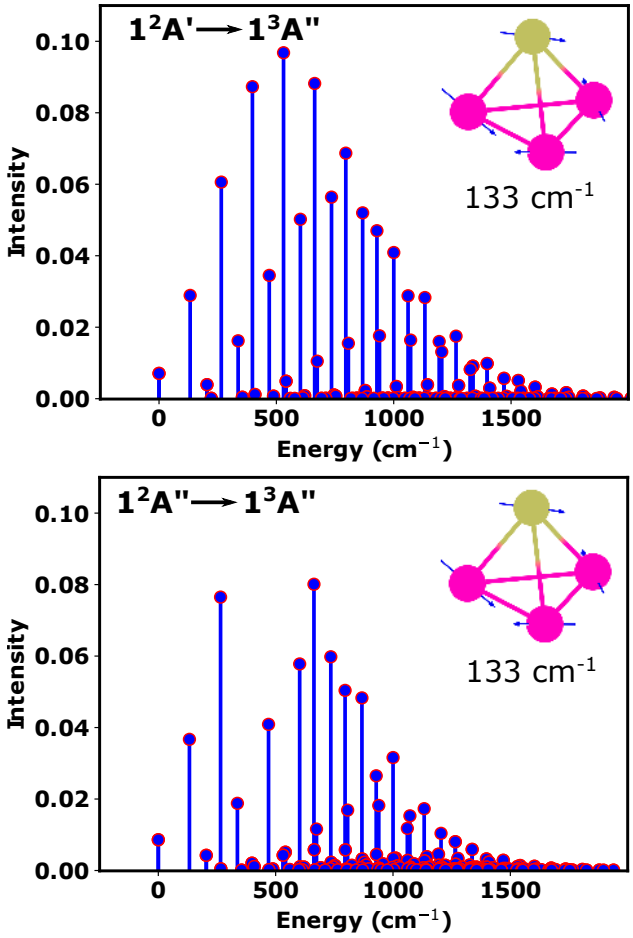

Figure 6: Franck-Condon factor simulations of two transitions from the two doublet ^{2}A' and ^{2}A" states to the triplet ^{3}A" state. Vibrational modes of the final state are presented in insets.

Conclusion

Geometries, ground and excited states, and electronic structures of the $TiGe_3^{-/0}$ clusters were studied by using relatively high levels of quantum chemical methods including TPSS, RCCSD(T)-F12, and CASSCF/CASPT2. The most stable geometrical structure of both

the anion and neutral were identified to have a tetrahedral arrangement of atoms. Due to a Jahn-Teller effect, the stable anionic cluster $TiGe_3^-$ cannot keep the highest possible symmetry (C_{3v}) of a tetrahedral η^3-$(Ge)_3Ti$ isomer but the C_s one. Conversely, the Jahn-Teller effect does not occur in the neutral ground state, and therefore its atomic tetrahedral cluster belongs to the spatial point group of C_{3v}.

The ground states of the anion and neutral play an important role in explanation of all visible bands in the experimental PE spectrum of $TiGe_3^-$. From the calculation results, two states of the anion (^{2}A' and ^{2}A") were identified to be nearly degenerate and competing for the anionic ground states on the potential energy hypersurface, and the a triplet state (^{3}A") was concluded to be the ground state of the neutral. As a result, these two states are expected to be populated in the experimental measurement process. On the basis the two experimetally populated states of the anion, multiple one-electron detachments were proven to underlie all visible bands in the anion photoelectron spectrum of $TiGe_3^-$. Particularly, five simultaneous one-electron removals from two anionic ground states were found to be responsible for the X band. The appearance of the A band in the spectrum was caused by two electronic transitions from the anionic states to two low-lying triplet ones. Further, the band B was ascribed to three deeper one-electron detachments. For the two higher bands C and D, each was attributed to two one-electron detachments originating from two competitive ground states of the anion. The highest visible band E could not be definitively assigned to specific electronic transitions due to highly demanding computation, but six detachments of one electron were predicted and are believed to give rise to this band and possible higher ones. Finally, Franck-Condon factor simulations of the two theoretically lowest electronic transitions unveiled that higher vibrational excited states of a harmonic vibrational mode has significant contributions to progression of the band X.

Acknowledgement

This work was supported by the Australian government through the Australian Research Council (ARC) under the Centre of Excellence scheme (project number CE170100026). It was also supported by computational resources provided by the Australian government through the National Computational Infrastructure National Facility (NCI_NF) and the Pawsey Supercomputer Centre.

ORCID

Le Nhan Pham: 0000-0001-9736-0747

Salvy P. Russo: 0000-0003-3589-3040

Note

The authors declare no competing financial interest

References

(1) Pillarisetty, R. Academic and industry research progress in germanium nanodevices. *Nature* **2011**, *479*, 324–328.

(2) Bals, S.; Van Aert, S.; Romero, C.; Lauwaet, K.; Van Bael, M. J.; Schoeters, B.; Partoens, B.; Yücelen, E.; Lievens, P.; Van Tendeloo, G. Atomic scale dynamics of ultrasmall germanium clusters. *Nat. Commun.* **2012**, *3*, 1–6.

(3) Martin, T.; Schaber, H. Mass spectra of Si, Ge, and Sn clusters. *J. Chem. Phys.* **1985**, *83*, 855–858.

(4) Liu, Y.; Zhang, Q.; Tittel, F. K.; Curl, R. F.; Smalley, R. E. Photodetachment and

photofragmentation studies of semiconductor cluster anions. *J. Chem. Phys.* **1986**, *85*, 7434–7441.

(5) Pacchioni, G.; Koutecký, J. Silicon and germanium clusters. A theoretical study of their electronic structures and properties. *J. Chem. Phys.* **1986**, *84*, 3301–3310.

(6) Hunter, J.; Fye, J.; Jarrold, M.; Bower, J. Structural transitions in size-selected germanium cluster ions. *Phys. Rev. Lett.* **1994**, *73*, 2063.

(7) Burton, G. R.; Xu, C.; Neumark, D. M. Study of small semiconductor clusters using anion photoelectron spectroscopy: germanium clusters (Ge_n, n = 2 – 15). *Surf. Rev. Lett.* **1996**, *3*, 383–388.

(8) Kumar, V.; Kawazoe, Y. Metal-encapsulated caged clusters of germanium with large gaps and different growth behavior than silicon. *Phys. Rev. Lett.* **2002**, *88*, 235504.

(9) Kumar, V.; Kawazoe, Y. Metal-encapsulated icosahedral superatoms of germanium and tin with large gaps: $Zn@Ge_{12}$ and $Cd@Sn_{12}$. *Appl. Phys. Lett.* **2002**, *80*, 859–861.

(10) Zhang, X.; Li, G.; Gao, Z. Laser ablation of Co/Ge mixtures: a new type of endohedral structure, a semiconductor cage trapping a metal atom. *Rapid Commun. Mass Spectrom.* **2001**, *15*, 1573–1576.

(11) Furuse, S.; Koyasu, K.; Atobe, J.; Nakajima, A. Experimental and theoretical characterization of MSi_{16}^-, MGe_{16}^-, MSn_{16}^-, and MPb_{16}^- (M= Ti, Zr, and Hf): The role of cage aromaticity. *J. Chem. Phys.* **2008**, *129*, 064311.

(12) Atobe, J.; Koyasu, K.; Furuse, S.; Nakajima, A. Anion photoelectron spectroscopy of germanium and tin clusters containing a transition-or lanthanide-metal atom; MGe_n^- (n= 8–20) and MSn_n^- (n= 15–17)(M= Sc–V, Y–Nb, and Lu–Ta). *Phys. Chem. Chem. Phys.* **2012**, *14*, 9403–9410.

(13) Deng, X.-J.; Kong, X.-Y.; Xu, X.-L.; Xu, H.-G.; Zheng, W.-J. Structural and magnetic properties of $CoGe_n^-$ (n= 2–11) clusters: Photoelectron spectroscopy and density functional calculations. *ChemPhysChem* **2014**, *15*, 3987–3993.

(14) Lu, S.-J.; Hu, L.-R.; Xu, X.-L.; Xu, H.-G.; Chen, H.; Zheng, W.-J. Transition from exohedral to endohedral structures of $AuGe_n^-$ (n= 2–12) clusters: Photoelectron spectroscopy and ab initio calculations. *Phys. Chem. Chem. Phys.* **2016**, *18*, 20321–20329.

(15) Espinoza-Quintero, G.; Duckworth, J. C.; Myers, W. K.; McGrady, J. E.; Goicoechea, J. M. Synthesis and characterization of $[Ru@Ge_{12}]^{3-}$: An endohedral 3-connected cluster. *J. Am. Chem. Soc.* **2014**, *136*, 1210–1213.

(16) Jin, Y.; Lu, S.; Hermann, A.; Kuang, X.; Zhang, C.; Lu, C.; Xu, H.; Zheng, W. Probing the structural evolution of ruthenium doped germanium clusters: Photoelectron spectroscopy and density functional theory calculations. *Sci. Rep.* **2016**, *6*, 30116.

(17) Wang, J.-Q.; Stegmaier, S.; Fässler, T. F. $[Co@Ge_{10}]^{3-}$: An intermetalloid cluster with archimedean pentagonal prismatic structure. *Angew. Chem., Int. Ed.* **2009**, *48*, 1998–2002.

(18) Deng, X.-J.; Kong, X.-Y.; Xu, H.-G.; Xu, X.-L.; Feng, G.; Zheng, W.-J. Photoelectron spectroscopy and density functional calculations of VGe_n^- (n= 3–12) clusters. *J. Phys. Chem. C* **2015**, *119*, 11048–11055.

(19) Deng, X.-J.; Kong, X.-Y.; Xu, X.-L.; Xu, H.-G.; Zheng, W.-J. Structural and bonding properties of small $TiGe_n^-$ (n= 2–6) clusters: photoelectron spectroscopy and density functional calculations. *RSC Adv.* **2014**, *4*, 25963–25968.

(20) Cramer, C. J.; Truhlar, D. G. Density functional theory for transition metals and transition metal chemistry. *Phys. Chem. Chem. Phys.* **2009**, *11*, 10757–10816.

(21) Dai, D.; Sumathi, K.; Balasubramanian, K. Eight electronic states and potential energy surfaces of Ge_3. *Chem. Phys. Lett.* **1992**, *193*, 251–257.

(22) Arnold, C. C.; Xu, C.; Burton, G. R.; Neumark, D. M. Study of the low-lying states of Ge_2 and Ge_2^- using negative ion zero electron kinetic energy spectroscopy. *J. Chem. Phys.* **1995**, *102*, 6982–6989.

(23) Pham, L. N.; Nguyen, M. T. Titanium digermanium: theoretical assignment of electronic transitions underlying its anion photoelectron spectrum. *J. Phys. Chem. A* **2017**, *121*, 1940–1949.

(24) Pham, L. N.; Nguyen, M. T. Insights into geometric and electronic structures of $VGe_3^{-/0}$ clusters from anion photoelectron spectrum Assignment. *J. Phys. Chem. A* **2017**, *121*, 6949–6956.

(25) Cohen, A. J.; Mori-Sánchez, P.; Yang, W. Fractional spins and static correlation error in density functional theory. *J. Chem. Phys.* **2008**, *129*, 121104.

(26) Cohen, A. J.; Mori-Sánchez, P.; Yang, W. Insights into current limitations of density functional theory. *Science* **2008**, *321*, 792–794.

(27) Jiang, W.; DeYonker, N. J.; Wilson, A. K. Multireference character for 3d transition-metal-containing molecules. *J. Chem. Theory Comput.* **2012**, *8*, 460–468.

(28) Wang, J.; Manivasagam, S.; Wilson, A. K. Multireference character for 4d transition metal-containing molecules. *J. Chem. Theory Comput.* **2015**, *11*, 5865–5872.

(29) Cohen, A. J.; Mori-Sánchez, P.; Yang, W. Challenges for density functional theory. *Chem. Rev.* **2012**, *112*, 289–320.

(30) Pham, L. N.; Hendrickx, M. F. Contributions of nearly-degenerate states to the photoelectron spectra of the vanadium dicarbide anion. *J. Phys. Chem. A* **2016**, *120*, 9465–9475.

(31) Pham, L. N.; Nguyen, M. T. Another Look at Photoelectron Spectra of the Anion $Cr_2O_2^-$: Multireference Character and Energetic Degeneracy. *J. Chem. Theory Comput.* **2018**, *14*, 4833–4843.

(32) Pham, L. N.; Nguyen, M. T. Electronic structure of neutral and anionic scandium disilicon $ScSi_2^{-/0}$ clusters and the related anion photoelectron spectrum. *J. Phys. Chem. A* **2016**, *120*, 9401–9410.

(33) Fdez. Galván, I.; Vacher, M.; Alavi, A.; Angeli, C.; Aquilante, F.; Autschbach, J.; Bao, J. J.; Bokarev, S. I.; Bogdanov, N. A.; Carlson, R. K. et al. OpenMolcas: From source code to insight. *J. Chem. Theory Comput.* **2019**, *15*, 5925–5964.

(34) Werner, H.-J.; Knowles, P. J.; Knizia, G.; Manby, F. R.; Schütz, M. Molpro: a general-purpose quantum chemistry program package. *Wiley Interdiscip. Rev.: Comput. Mol. Sci.* **2012**, *2*, 242–253.

(35) TURBOMOLE V7.2 2017, a development of University of Karlsruhe and Forschungszentrum Karlsruhe GmbH, 1989-2007, TURBOMOLE GmbH, since 2007; available from http://www.turbomole.com. (Accessed April 30, 2020).

(36) Andersson, K.; Malmqvist, P.-Å.; Roos, B. O. Second-order perturbation theory with a complete active space self-consistent field reference function. *J. Chem. Phys.* **1992**, *96*, 1218–1226.

(37) Roos, B. O.; Lindh, R.; Malmqvist, P.-Å.; Veryazov, V.; Widmark, P.-O. New relativistic ANO basis sets for transition metal atoms. *J. Phys. Chem. A* **2005**, *109*, 6575–6579.

(38) Roos, B. O.; Lindh, R.; Malmqvist, P.-Å.; Veryazov, V.; Widmark, P.-O. Main group atoms and dimers studied with a new relativistic ANO basis set. *J. Phys. Chem. A* **2004**, *108*, 2851–2858.

(39) Adler, T. B.; Knizia, G.; Werner, H.-J. A simple and efficient CCSD(T)-F12 approximation. *J. Chem. Phys.* **2007**, *127*, 221106.

(40) Tao, J.; Perdew, J. P.; Staroverov, V. N.; Scuseria, G. E. Climbing the density functional ladder: Nonempirical meta–generalized gradient approximation designed for molecules and solids. *Phys. Rev. Lett.* **2003**, *91*, 146401.

(41) Balabanov, N. B.; Peterson, K. A. Systematically convergent basis sets for transition metals. I. All-electron correlation consistent basis sets for the 3d elements Sc–Zn. *J. Chem. Phys.* **2005**, *123*, 064107.

(42) Wilson, A. K.; Woon, D. E.; Peterson, K. A.; Dunning, T. H. Gaussian basis sets for use in correlated molecular calculations. IX. The atoms gallium through krypton. *J. Chem. Phys.* **1999**, *110*, 7667–7676.

(43) Reiher, M.; Wolf, A. Exact decoupling of the Dirac Hamiltonian. II. The generalized Douglas–Kroll–Hess transformation up to arbitrary order. *J. Chem. Phys.* **2004**, *121*, 10945–10956.

(44) Weigend, F.; Ahlrichs, R. Balanced basis sets of split valence, triple zeta valence and quadruple zeta valence quality for H to Rn: Design and assessment of accuracy. *Phys. Chem. Chem. Phys.* **2005**, *7*, 3297–3305.

(45) Borrelli, R.; Capobianco, A.; Peluso, A. Franck–Condon factors—Computational approaches and recent developments. *Can. J. Chem.* **2013**, *91*, 495–504.

TOC Graphic